Available online at www.sciencedirect.com
ScienceDirect
International Journal of Heat and Mass Transfer 49 (2006) 4821–4830
International Journal of HEAT and MASS TRANSFER
www.elsevier.com/locate/ijhmt

Buoyancy convection in cylindrical conducting melt with low Grashof number under uniform static magnetic field

Yuko Inatomi *

Institute of Space and Astronautical Science, Japan Aerospace Exploration Agency, 3-3-1 Yoshinodai, Sagamihara, Kanagawa 229-8510, Japan

Received 11 January 2006; received in revised form 1 June 2006
Available online 8 August 2006

Abstract

Damping of convection is key in the precise measurement of a diffusion coefficient in melt, and applying a static magnetic field to the melt is a promising method of realizing damping in electrically conducting melt such as a semiconductor and metal. Convection behavior in a melt with a low Grashoff number under a uniform static magnetic field was calculated on the basis of the finite element method. Using the results, the specimen geometry and the direction of the applied magnetic field in diffusion experiments with a diffusion-couple method were evaluated by the numerical simulation.

Keywords: Static magnetic field; Natural convection; Diffusion coefficient; Numerical simulation; Electrically conducting melt

1. Introduction

In spite of the importance of understanding diffusion phenomena of solute atoms in liquid from the viewpoint of crystal growth and solidification, there may be few reliable values on diffusion coefficients in liquid obtained in a terrestrial environment. The reason is experimental difficulties in measurement, e.g., diffusion during heating and cooling processes, and mixing by convection in the liquid. The heating and cooling periods must be much shorter than the diffusion period. The former difficulty has been overcome by adopting a shear-cell method [1] and a rapid-quench capillary method [2]. On the other hand, it is not easy to solve the latter, because temperature and concentration gradients in the liquid become driving forces of convection and the convection influences the concentration field. Therefore, the achievement of a diffusion-dominated condition in the liquid is regarded to be a promising method for enabling measurement. Many diffusion experiments were performed in a microgravity environment in order to confirm the difference in diffusion coefficients obtained in a microgravity environment from those obtained in the terrestrial environment. Those studies verified the difference between the two. More interestingly, the temperature dependence of diffusion coefficients in a microgravity environment was different from that in a terrestrial environment [3–6]. However, long-duration microgravity experiments on board a space shuttle or a satellite are now difficult to conduct, and moreover, the short-duration microgravity condition, such as that achieved in a drop shaft or on parabolic flights of an airplane is not favorable for the diffusion experiment.

When a uniform static magnetic field is applied to an electrically conducting liquid, liquid motion is reduced because of the Lorentz force yielded by interaction between the imposed magnetic induction and the electric current induced by the field [7,8]. There have been some reports concerning the measurement of interdiffusion coefficients under a static magnetic field [2,9,10]. However, the influence of the applied magnetic induction and the gravity on the flow behavior in the melt were discussed based merely on the measured diffusion coefficients or analytical estimation. The purpose of the present study is to evaluate the suitable condition under which to damp the

* Tel.: +81 42 759 8529; fax: +81 42 759 8530.
E-mail address: inatomi@isas.jaxa.jp

0017-9310/$ - see front matter © 2006 Elsevier Ltd. All rights reserved.
doi:10.1016/j.ijheatmasstransfer.2006.06.002

Nomenclature

$\boldsymbol{a}$ unit vector parallel to specimen axis (–)
A aspect ratio of melt, L/r (–)
$\boldsymbol{b}$ uniform applied magnetic induction vector (T)
b_0 $|\boldsymbol{b}|$ (T)
$\boldsymbol{B}$ nondimensional magnetic induction vector, $\boldsymbol{b}/b_0$ (–)
$c(x,y,z,\tau)$ solute concentration in melt (at.%)
c_0, c_1 initial values of c at $t=0$ for $Z<0$ and for $Z>0$ (at.%)
$C(X,Y,Z,t)$ $(c-c_0)/\Delta c$ (–)
D diffusion coefficient of solute atom in melt ($m^2\ s^{-1}$)
$\boldsymbol{g}$ gravity vector ($m\ s^{-2}$)
g_0 $|\boldsymbol{g}|$ ($m\ s^{-2}$)
$\boldsymbol{G}$ nondimensional gravitational acceleration, $\boldsymbol{g}/g_0$ (–)
Gr Grashof number, $\beta_T g_0 \Delta\Theta r^3/A\nu^2$ (–)
Ha Hartmann number, $b_0 r(\sigma/\rho_0\nu)^{1/2}$ (–)
$\boldsymbol{J}$ nondimensional electric current density (–)
L half-length of melt (m)
$p(x,y,z,\tau)$ pressure (Pa)
$P(X,Y,Z,t)$ nondimensional pressure, $p/\rho_0 U_0^2$ (–)
Pr Prandtl number, ν/κ (–)
r radius of melt (m)
Sc Schmidt number, ν/D (–)
t nondimensional time, $D\tau/r^2$ (–)
$T(X,Y,Z,t)$ nondimensional temperature, $(\Theta-\Theta_0)/\Delta\Theta$ (–)
$\boldsymbol{u}(x,y,z,\tau)$ flow velocity vector in melt ($m\ s^{-1}$)
$\boldsymbol{U}(X,Y,Z,t)$ nondimensional flow velocity vector, $\boldsymbol{u}/U_0=(U_X,U_Y,U_Z)$ (–)
U_0 characteristic velocity in melt, $\nu Gr^{1/2}/r$ ($m\ s^{-1}$)
$U_{max}(Ha,t)$ magnitude of maximum velocity in melt as a function of Ha and t (–)
$U_{max,st}(Ha)$ $U_{max}(Ha,t)$ with a steady state as a function of Ha (–)
x, y, z Cartesian coordinates (m)
X, Y, Z x/r, y/r, z/r (–)

Greek symbols
α nondimensional solute volume expansion coefficients, $\beta_S\Delta c/\beta_T\Delta\Theta$ (–)
β_S, β_T solute and thermal volume expansion coefficients (K^{-1})
Δc c_1-c_0 (at.%)
$\Delta\Theta$ $\Theta_1-\Theta_0$ (K)
$\Theta(x,y,z,\tau)$ temperature (K)
Θ_0, Θ_1 temperature in melt at $Z=\pm A$ and $Z=0$ with $(X^2+Y^2)^{1/2}=1$ (K)
κ thermal diffusivity of melt ($m^2\ s^{-1}$)
ν kinematic viscosity of melt ($m^2\ s^{-1}$)
ρ_0 density of melt for $\Theta=\Theta_1$ and $c=c_0$ ($kg\ m^{-3}$)
σ electrical conductivity of melt ($\Omega^{-1}\ m^{-1}$)
τ time (s)
$\phi(X,Y,Z,t)$ nondimensional electric potential, Ψ/b_0U_0r (–)
$\Psi(x,y,z,\tau)$ electric potential (V)
∇_N, ∇_N^2 $\mathbf{i}\partial/\partial X+\boldsymbol{j}\partial/\partial Y+\boldsymbol{k}\partial/\partial Z$, $\boldsymbol{i}\partial^2/\partial X^2+\boldsymbol{j}\partial^2/\partial Y^2+\boldsymbol{k}\partial^2/\partial Z^2$ (–)

convection in order to measure a reliable diffusion coefficient in electrically conducting melt under a terrestrial condition, utilizing a static magnetic field based on a numerical simulation. The direction and the magnitude of magnetic induction, and the aspect ratio of the container were regarded to be parameters for controlling the damping effect.

2. Mathematical model

Liquid metal usually conducts electricity and Lorentz force is induced in the melt upon the application of a magnetic field, which can be employed to control convection. The liquid metal is assumed to be sealed in an electrically insulated container. The Navier–Stokes equation including the effect of Lorentz force for an incompressible fluid in the Boussinesq approximation can be written with the aid of Ohm's law and the continuity of electric current density in the present simulation. The effects of the displacement current and Joule heating in the melt are neglected in the basic equations. Thermocapillary flow and other effects attributed to a magnetic field were not taken into consideration in the equations. The magnetic induction vector in the melt can be set equal to the uniform applied magnetic field and the electric field can be written as the gradient of an electric potential, when the magnetic Reynolds number is much smaller than unity. Electrical conductivity and the viscosity of the melt are assumed to be constant. The following basic equations can be obtained as nondimensional forms under the above assumptions.

Equation of electric potential

Nondimensional electric current density $\boldsymbol{J}$ in the melt is given by Ohm's law as

$$\boldsymbol{J}=-\nabla_N\phi+\boldsymbol{U}\times\boldsymbol{B}. \tag{1}$$

The equation of continuity for $\boldsymbol{J}$ is

$$\nabla_N\cdot\boldsymbol{J}=0. \tag{2}$$

The equation of electric potential is then given by the above equations as follows:

$$-\nabla_N^2\phi+\boldsymbol{B}\cdot(\nabla_N\times\boldsymbol{U})=0. \tag{3}$$

Equation of continuity

$$\nabla_N \cdot \boldsymbol{U} = 0. \tag{4}$$

Equation of momentum conservation

$$\frac{1}{Sc}\frac{\partial \boldsymbol{U}}{\partial t} + \sqrt{Gr}(\boldsymbol{U}\cdot\nabla_N)\boldsymbol{U} = -\nabla_N P + \nabla_N^2 \boldsymbol{U} - A\sqrt{Gr}(T+\alpha C)\boldsymbol{G} - Ha^2 \boldsymbol{J}\times\boldsymbol{B}. \tag{5}$$

Energy equation

$$Pr\left[\frac{1}{Sc}\frac{\partial T}{\partial t} + \sqrt{Gr}(\boldsymbol{U}\cdot\nabla_N)T\right] = \nabla_N^2 T. \tag{6}$$

The Joule heat term is ignored in Eq. (6) because of the small current density in the melt.

Species equation

$$\frac{\partial C}{\partial t} + Sc\sqrt{Gr}(\boldsymbol{U}\cdot\nabla_N)C = \nabla_N^2 C. \tag{7}$$

Boundary conditions

The schematic drawing of the model system used in the calculation is shown in Fig. 1. Only a half-section of the cylindrical melt is modeled due to the symmetry at the X–Z plane. The walls of the container are electrically insulated from the surroundings and satisfied no-slip conditions. The mass flux at the walls is zero. On all the walls of the container, $(X^2+Y^2)^{1/2}=1$, $Z=\pm A$:

$$\boldsymbol{U} = \boldsymbol{0}, \tag{8}$$

$$\boldsymbol{J}\cdot\boldsymbol{n} = 0, \tag{9}$$

$$\nabla_N C\cdot\boldsymbol{n} = 0, \tag{10}$$

$$\nabla_N T\cdot\boldsymbol{n} = 0. \tag{11}$$

For simplicity, the temperature distribution on the side wall is set to be a power-law function of Z along the wall, $(X^2+Y^2)^{1/2}=1$:

$$T = -(Z/A)^n. \tag{12}$$

The isothermal condition is applied to the each end of the melt, because the high thermal conductivity of the melt may be sufficient to decrease the temperature gradient on the faces. On each end of the container $Z=\pm A$:

$$T = -1. \tag{13}$$

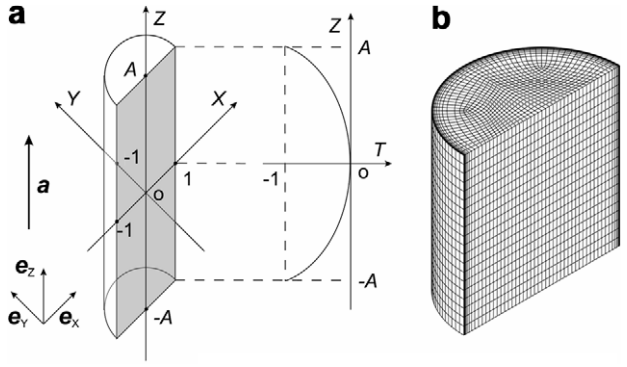

Fig. 1. Model system used in calculation: (a) geometry of semi-cylindrical cavity and coordinates, (b) element representation of graded 3D-mesh for cavity with $A=1$.

On the symmetry plane $Y=0$:

$$U_Y = 0, \tag{14}$$

$$\partial T/\partial Y = 0, \tag{15}$$

$$\partial \phi/\partial Y = 0. \tag{16}$$

Initial conditions

$$\boldsymbol{U} = \boldsymbol{0}, \tag{17}$$

$$\phi = 0, \tag{18}$$

$$\boldsymbol{J} = \boldsymbol{0}, \tag{19}$$

$$T = -(Z/A)^n, \tag{20}$$

$$C(X,Y,Z,0) = C_{\text{init}}(X,Y,Z). \tag{21}$$

3. Computational scheme

Numerical simulations were performed using the commercial software package FIDAP 8.6 [11], which is based on the finite element method. All calculations were carried out with a nonuniform four-node quadrilateral element mesh for the contents in the container. The computations for the cases with A =1, 5 and 10 were carried out with three different element systems, 23,520 elements, 117,600 elements and 235,200 elements, respectively. Volumetric forces such as gravity and Lorentz forces were applied to the fluid following Eq. (5). A user-defined subroutine was coded to build the source term of the electric charge into Eq. (3). The direction of the specimen axis was set to be parallel to $\boldsymbol{e}_Z$. Hereafter, the direction of normalized gravity $\boldsymbol{G}$ parallel to $\boldsymbol{e}_X$, $\boldsymbol{e}_Y$ or $\boldsymbol{e}_Z$ is referred to as $\boldsymbol{G}\|\boldsymbol{e}_X$, $\boldsymbol{G}\|\boldsymbol{e}_Y$ or $\boldsymbol{G}\|\boldsymbol{e}_Z$, respectively. A uniform static magnetic field was applied parallel to $\boldsymbol{e}_X$, $\boldsymbol{e}_Y$ or $\boldsymbol{e}_Z$. As in the above description of gravity, the magnetic induction vectors parallel to $\boldsymbol{e}_X$, $\boldsymbol{e}_Y$ and $\boldsymbol{e}_Z$ are referred to as $\boldsymbol{B}\|\boldsymbol{e}_X$, $\boldsymbol{B}\|\boldsymbol{e}_Y$ and $\boldsymbol{B}\|\boldsymbol{e}_Z$, respectively. The directions of $\boldsymbol{G}\|\boldsymbol{e}_X$ and $\boldsymbol{G}\|\boldsymbol{e}_Z$ were chosen by taking account of the symmetry of the melt.

In the present calculation, physical properties of metal and semiconductor melts [12] were assumed to be as follows: density $\rho_0 = 5\times10^3\ \text{kg/m}^3$, kinematic viscosity $\nu = 10^{-7}\ \text{m}^2\,\text{s}^{-1}$, thermal volume expansion coefficient $\beta_T = 10^{-4}\ \text{K}^{-1}$, solute volume expansion coefficient $\beta_S = 10^{-4}\ \text{at.}\%^{-1}$, electrical conductivity $\sigma = 10^6\ \Omega^{-1}\,\text{m}^{-1}$, thermal diffusivity $\kappa = 10^{-5}\ \text{m}^2\,\text{s}^{-1}$, diffusion coefficient of solute atom in melt $D = 10^{-9}\ \text{m}^2\,\text{s}^{-1}$, radius of the specimen $r = 10^{-3}$ m, aspect ratio $A = 10$, temperature difference $\Delta\Theta = 1$ K, and applied magnetic induction $b_0 = 1$ T. Therefore, nondimensional parameters Pr, Sc, Gr and Ha corresponding to the properties were calculated to be 10^{-2}, 10^2, 10 and 40, respectively.

4. Results and discussion

4.1. Computed results for thermal convection under steady-state condition

Thermal convection under a uniform magnetic field was investigated by changing $\boldsymbol{G}$, $\boldsymbol{B}$, and A. Initial concentration

$C_{\text{init}}(X, Y, Z)$ in Eq. (21) is set to be zero and A is chosen to be 1, 5 or 10. Transition of flow behavior from laminar to oscillatory does not occur under the calculation condition, and the velocity, temperature and electrical potential profiles converge to the steady state. The temperature distributions in the melt for $\boldsymbol{G}\|\boldsymbol{e}_Z$ and $\boldsymbol{G}\|\boldsymbol{e}_X$ are not influenced by convection because of the low Gr, i.e., these temperature fields are governed by conductive heat transfer. When the curl operators are applied to Eq. (5) to eliminate the pressure gradient term, the following equation is obtained under the steady-state condition at $Ha = 0$:

$$\nabla_N^2\left[\nabla_N \times \left(\frac{1}{\sqrt{Gr}}\boldsymbol{U}\right)\right] - Gr\nabla_N \times \left[\left(\frac{1}{\sqrt{Gr}}\boldsymbol{U}\cdot\nabla_N\right)\left(\frac{1}{\sqrt{Gr}}\boldsymbol{U}\right)\right] = A\nabla_N(T+\alpha C)\times\boldsymbol{G}. \quad (22)$$

If $|A\nabla_N T \times \boldsymbol{G}|$ is small enough to neglect the second term in the left side of Eq. (22), $\boldsymbol{U}/\sqrt{Gr}$ is dominated by $A\nabla_N(T+\alpha C)\times\boldsymbol{G}$. Table 1 shows the magnitude of maximum velocity in the melt divided by $Gr^{1/2}$ in a steady state at $Ha = 0$, $U_{\max,\text{st}}(0)/Gr^{1/2}$, as a function of A and Gr with $n = 2$. Since $U_{\max,\text{st}}(0)/Gr^{1/2}$ is almost constant for the same A with Gr in a range of between 1 and 100, the convection term is negligible in Eq. (5). $U_{\max,\text{st}}(0)/Gr^{1/2}$ increases with the increase of A for $\boldsymbol{G}\|\boldsymbol{e}_X$, whereas the magnitude of the maximum velocity decreases with the increase of A for $\boldsymbol{G}\|\boldsymbol{e}_Z$. An isotherm plot for the melt at $Ha = 0$ is shown in Fig. 2, and the temperature distribution for $A = 1$, 5 or 10 is not influenced by the convection because of the low Gr. The distribution of $A\nabla_N T \times \boldsymbol{G}$ in the melt has a very weak Gr dependence. The maximum temperature gradient appears along the circumferences of both ends of the melt $(X^2 + Y^2)^{1/2} = 1$ at $Z = \pm A$. For $\boldsymbol{G}\|\boldsymbol{e}_X$, $U_{\max,\text{st}}(0)/Gr^{1/2}$ is determined by the maximum temperature gradient parallel to the Z axis, and increases with the increase of A on the axis, because $|A\nabla_N T \times G|$ on the melt axes, $X = Y = 0$ at $Z = \pm A$, for $A = 1$, 5 and 10 are, respectively, 1.23, 1.98 and 1.99, whereas those on the circumferences are 2.00 for all A's. For $\boldsymbol{G}\|\boldsymbol{e}_Z$, $U_{\max,\text{st}}(0)/Gr^{1/2}$ is determined by the maximum radial temperature gradient which appears on the circumference of the $Z = 0$ plane of the melt. $|A\nabla_N T \times \boldsymbol{G}|$ on the melt axes for $A = 1$, 5 and 10 are, respectively, 0.812, 0.199 and 0.0997, and therefore $U_{\max,\text{st}}(0)/Gr^{1/2}$ decreases with the increase of A. Consequently, the minimum value of $U_{\max,\text{st}}(0)$ with Gr in the range of between 1 and 100 is achieved under the condition of $\boldsymbol{G}\|\boldsymbol{e}_Z$ with $A = 10$.

Table 1
$U_{\max,\text{st}}(0)/Gr^{1/2}$ as a function of A and Gr for $n = 2$

Direction of $\boldsymbol{G}$	A	$U_{\max,\text{st}}(0)/Gr^{1/2}$		
		$Gr = 1$	$Gr = 10$	$Gr = 100$
$\boldsymbol{G}\|\boldsymbol{e}_X$	1	9.35×10^{-3}	9.32×10^{-3}	9.33×10^{-3}
	5	6.26×10^{-2}	6.28×10^{-2}	6.28×10^{-2}
	10	7.71×10^{-2}	7.69×10^{-2}	7.60×10^{-2}
$\boldsymbol{G}\|\boldsymbol{e}_Z$	1	6.60×10^{-3}	6.61×10^{-3}	6.60×10^{-3}
	5	2.08×10^{-3}	2.07×10^{-3}	2.08×10^{-3}
	10	1.03×10^{-3}	1.03×10^{-3}	1.04×10^{-3}

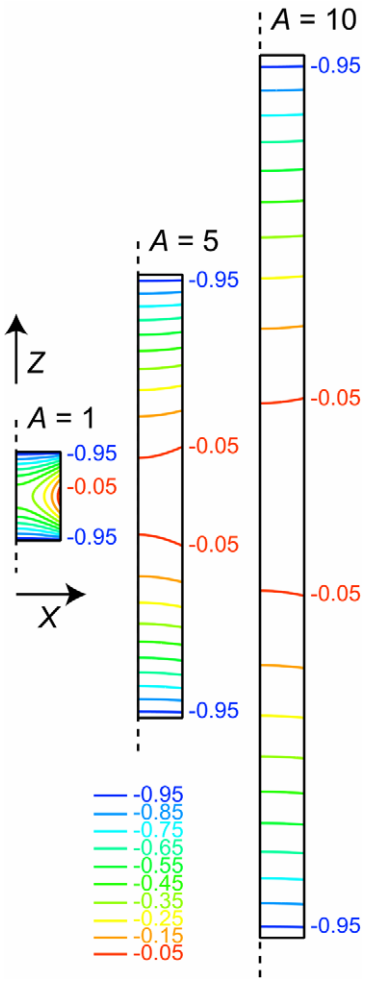

Fig. 2. Isotherm plot for melt under condition of $Gr = 0$ with $n = 2$ and $Ha = 0$.

$U_{\max,\text{st}}(Ha)$ decreases monotonically with the increase of Ha due to the flow damping effect of the Lorentz force, as shown in Fig. 3. $U_{\max,\text{st}}(Ha)$ becomes smaller with the increase of A for $\boldsymbol{B}\|\boldsymbol{e}_Z$, while $U_{\max,\text{st}}(Ha)$ with $A = 1$ for $\boldsymbol{B}\|\boldsymbol{e}_X$ is almost similar to that for $\boldsymbol{B}\|\boldsymbol{e}_Z$. By applying magnetic induction at $Ha = 40$ and 200, $U_{\max,\text{st}}(Ha)$'s for both cases are damped similar to those under low-gravity accelerations of $1.6 \times 10^{-3} g_0$ and $1.6 \times 10^{-5} g_0$, respectively. Fig. 4 shows the calculated results of contour plots for the magnitude of the velocity, $|\boldsymbol{U}|/U_{\max,\text{st}}(Ha)$, on X–Z and Y–Z planes at $Ha = 40$ for $\boldsymbol{G}\|\boldsymbol{e}_Z$ with $A = 1$, 5 and 10, where $U_{\max,\text{st}}(Ha)$ is shown in Fig. 3. Convective roll arises along the melt axis at $Ha = 0$, and the roll shifts to the circumference of the melt with the increase of Ha, because the driving force of convection at the circumference is greater than that on the melt axis, as mentioned above.

The difference in the damping effect between $\boldsymbol{B}\|\boldsymbol{e}_Z$ and $\boldsymbol{B}\|\boldsymbol{e}_X$ conditions can be explained as follows. The Lorentz force affects the flow perpendicular to the specimen axis in the vicinity of $Z = \pm A$ for $\boldsymbol{B}\|\boldsymbol{e}_Z$. On the other hand,

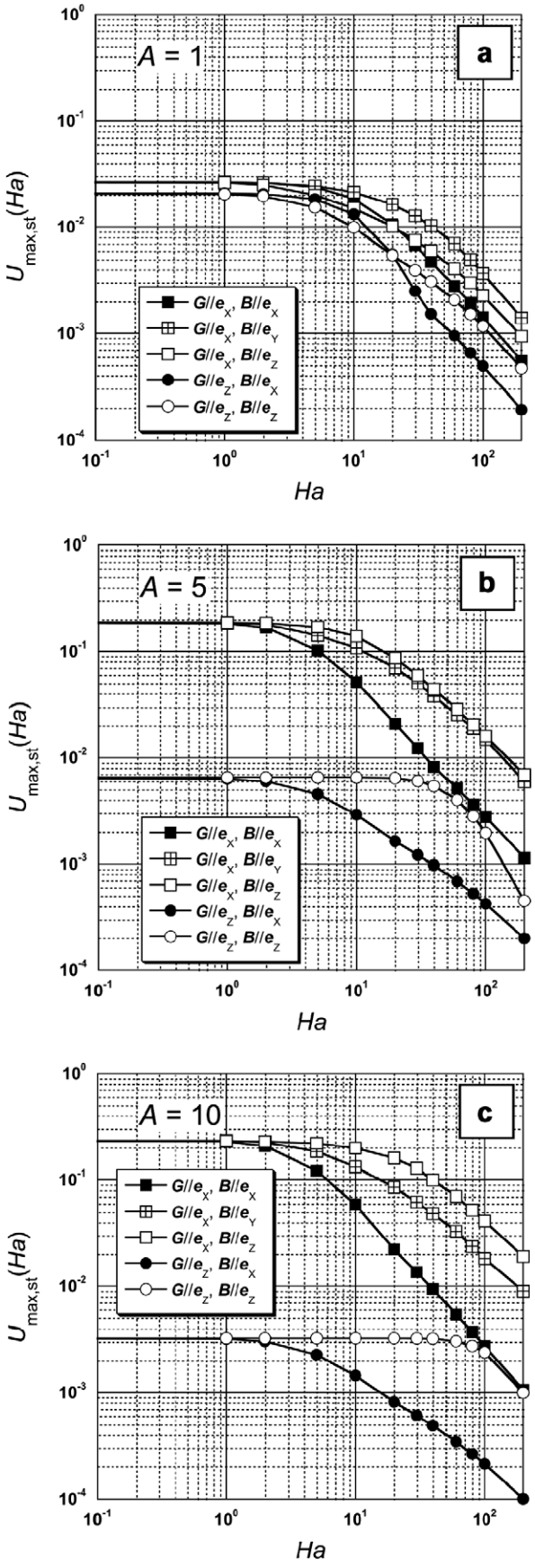

Fig. 3. $U_{max,st}(Ha)$ for $Gr = 10$ with $n = 2$.

the force affects the flow parallel to the specimen axis in the middle region for $\boldsymbol{B}\|\boldsymbol{e}_X$. The region dominated by the flow in the vicinity of the $Z = \pm A$ surface for $A = 1$ has nearly the same volumes as does that of the middle region, and therefore the damping effect has no obvious dependence on the direction of the applied magnetic field. The volume of the former region becomes smaller relative to the total volume with the increase of aspect ratio, and consequently, the damping effect for $\boldsymbol{B}\|\boldsymbol{e}_Z$ becomes smaller than that for $\boldsymbol{B}\|\boldsymbol{e}_X$. Fig. 5 shows the contour plots of normalized Lorentz force $|\boldsymbol{J} \times \boldsymbol{B}|/JB_{max}$ on X–Z and Y–Z planes at $Ha = 40$ for $\boldsymbol{G}\|\boldsymbol{e}_Z$ with $A = 1$, 5 and 10, where JB_{max} is the maximum magnitude of the vector product $\boldsymbol{J} \times \boldsymbol{B}$ in melt. For $\boldsymbol{B}\|\boldsymbol{e}_X$, the Lorentz force near the melt axis is almost parallel to the axis, and the Z dependence of the Lorentz force is very weak in the vicinity of the $Z = 0$ plane. Since the flow near the $Z = \pm A$ surface has anisotropic radial components, it is damped by anisotropic Lorentz forces. For $\boldsymbol{B}\|\boldsymbol{e}_Z$, the Lorentz force does not appear near the $Z = 0$ plane, because the flow direction is almost parallel to $\boldsymbol{B}$. The damping effect of Lorentz force is yielded only in the vicinity of the $Z = \pm A$ surface. It must be noticed that the electrical field vanishes in Eq. (1) for axisymmetric flow under an axial magnetic field in an electrically insulated container [13]. Therefore, the damping effect of Lorentz force for $\boldsymbol{B}\|\boldsymbol{e}_Z$ with large A is weaker than that for $\boldsymbol{B}\|\boldsymbol{e}_X$, because the region where Lorentz force affects the flow behavior is small, whereas the current density $\boldsymbol{J}$ for $\boldsymbol{B}\|\boldsymbol{e}_Z$ is higher than that for $\boldsymbol{B}\|\boldsymbol{e}_X$.

Although the temperature distribution along the container wall was assumed to be the square law of Z, we must consider the case with a higher n value, taking account of the influence of the configuration of the heater and the container on the temperature distribution. $U_{max,st}(Ha)$ for $\boldsymbol{G}\|\boldsymbol{e}_Z$, $A = 10$, and $Gr = 10$ with $n = 2$, 4, and 6 is shown in Fig. 6, where $U_{max,st}(0)$'s for $n = 2$, 4, 6 are 3.3×10^{-3}, 1.1×10^{-2} and 2.4×10^{-2}, respectively. As the n value increases, the local temperature gradient in the melt increases and thus $U_{max,st}(0)$ increases. However, $U_{max,st}(Ha)$ is insensitive to the n value for $\boldsymbol{B}\|\boldsymbol{e}_X$, though the dependence is obviously sensitive to the n value for $\boldsymbol{B}\|\boldsymbol{e}_Z$. As a result, the minimum value of the normalized maximum velocity is achieved for $\boldsymbol{B}\|\boldsymbol{e}_X$ with $\boldsymbol{G}\|\boldsymbol{e}_Z$ regardless of the n value.

4.2. Computed results for mass transport in transient state

The diffusion coefficient of a solute atom in melt D has been experimentally determined from the concentration profile along the specimen axis by the capillary method, diffusion-couple method, or shear-cell method. Damping of convection in melt is effective for improving the measurement accuracy of the coefficient. It was described in Section 4.1 that the damping effect of a magnetic field on convection is obvious for $\boldsymbol{B}\|\boldsymbol{e}_X$ with large A. The large A is also preferable for the measurement, because

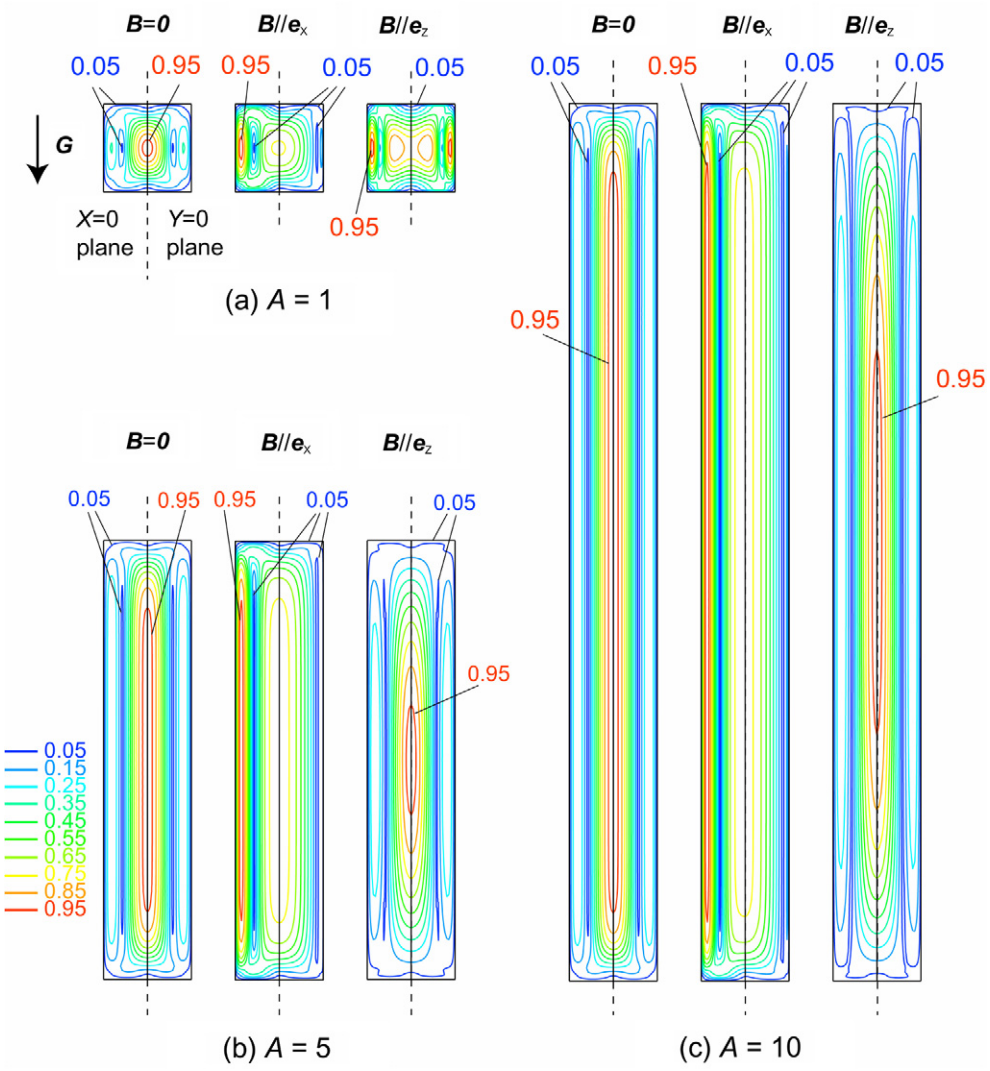

Fig. 4. Contour plot of magnitude of velocity, $|\boldsymbol{U}|/U_{\max,\mathrm{st}}(Ha)$, on $X=0$ and $Y=0$ planes under condition of $Gr=10$ with $n=2$, $Ha=40$, and $\boldsymbol{G}\|\boldsymbol{e}_Z$.

the coefficient is usually calculated through comparison of the measured distribution with the solution of a diffusion equation by a curve-fitting method. In this section, the transport of the solute atom under a magnetic field will be discussed under the conditions of $Gr=10$ and 100 with $A=10$, $n=2$, $\boldsymbol{G}\|\boldsymbol{e}_Z$, and $\boldsymbol{B}\|\boldsymbol{e}_X$.

Mass transport in melt without convection in a one-dimensional system is described as the following equation derived from Eq. (7) with $\boldsymbol{U}=\boldsymbol{0}$:

$$\frac{\partial C}{\partial t}=\frac{\partial^2 C}{\partial Z^2}. \tag{23}$$

For the diffusion-couple method, $C(Z,t)$ is obtained using the Fourier series by solving Eq. (23) with the boundary condition $(\partial C/\partial Z)_{Z=-A}=(\partial C/\partial Z)_{Z=A}=0$ and the initial conditions $C(-A,0)=0$, $C(0,0)=1/2$ and $C(A,0)=1$, as follows:

$$C(Z,t)=\frac{1}{2}+\frac{1}{A}\sum_{n=1}^{\infty}\left[\frac{1}{a_n}\sin(a_nZ)\exp(-a_n^2t)\right], \tag{24a}$$

$$a_n=\frac{2n-1}{2A}\pi. \tag{24b}$$

The concentration gradient along the Z direction at $Z=0$, $G_{\mathrm{C}}(t)=(\partial C/\partial Z)_{Z=0}$, is derived from Eq. (24) as

$$G_{\mathrm{C}}(t)=\frac{1}{A}\sum_{n=1}^{\infty}\exp(-a_n^2t)\approx\frac{1}{2\sqrt{\pi t}}\quad\text{for } t\ll A^2/4. \tag{25}$$

Thus, the diffusion coefficient D can be approximated as $r^2/4\pi\tau G_{\mathrm{C}}^2$ for small t, if G_{C} is measured experimentally under the no-convection condition. The concentration distribution in the X–Y plane is, however, usually inhomogeneous due to mixing by buoyancy convection under the terrestrial condition. The concentration gradient on the $Z=0$ plane obtained experimentally after quenching the melt is averaged in the cross-section of the melt by

$$G_{\mathrm{C}}^{*}(t)=\frac{1}{\pi}\int_{Z=0}(\nabla_N C\cdot\boldsymbol{a})\mathrm{d}S. \tag{26}$$

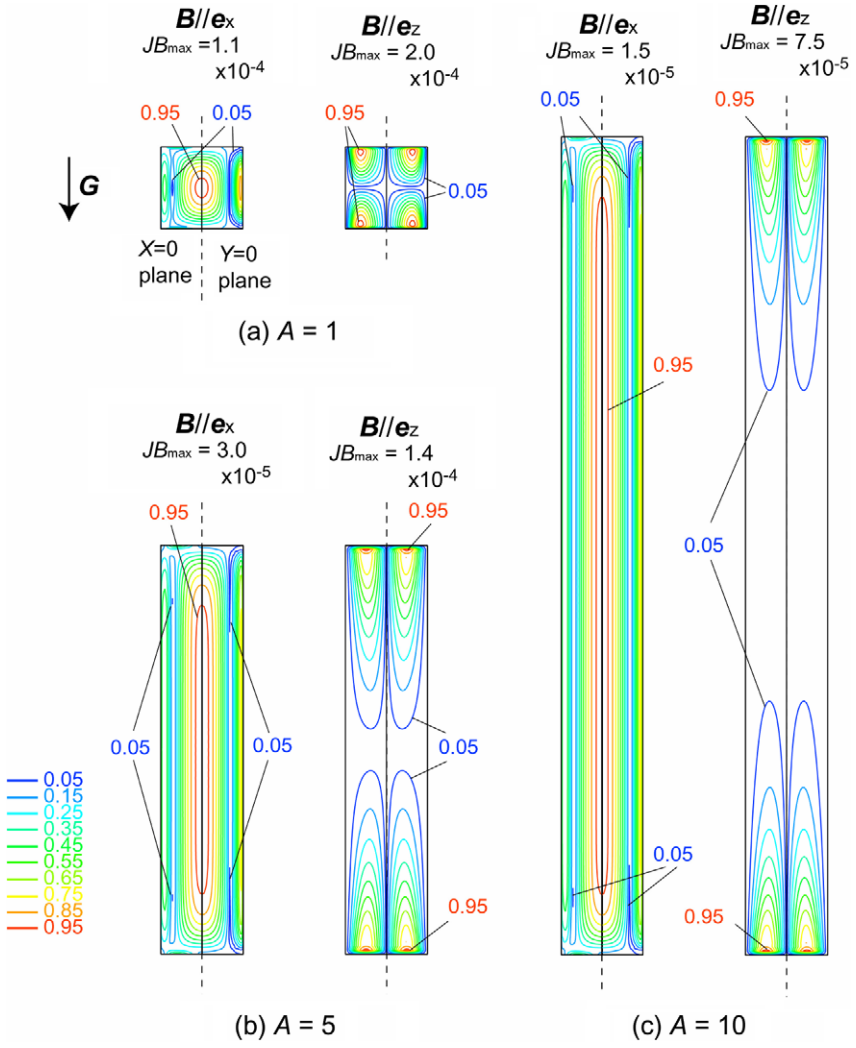

Fig. 5. Contour plot of Lorentz force on $X = 0$, $Y = 0$ and $Z = 0$ planes under condition of $Gr = 10$ with $n = 2$, $Ha = 40$, and $\boldsymbol{G} \| \boldsymbol{e}_Z$.

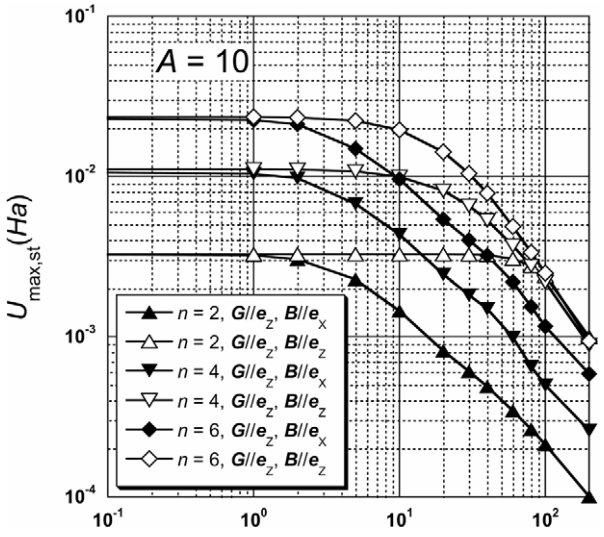

Fig. 6. $U_{\max,\mathrm{st}}(Ha)$ for $Gr = 10$ with $n = 2$, 4 and 6.

The initial concentration C_{init} for the calculation is defined by taking account of the half-width of the transient region δ as follows:

$$C_{\mathrm{init}}(X, Y, Z) = 0 \quad \text{at} \quad -A \leqslant Z \leqslant -\delta, \tag{27a}$$

$$C_{\mathrm{init}}(X, Y, Z) = \frac{1}{2}\left(1 + \frac{1}{\delta}Z\right) \quad \text{at} \quad -\delta < Z < \delta, \tag{27b}$$

$$C_{\mathrm{init}}(X, Y, Z) = 1 \quad \text{at} \quad \delta \leqslant Z \leqslant A. \tag{27c}$$

An alloy with a high solute concentration must be set in the region $0 < Z \leqslant A$ in the diffusion couple for $\beta_S > 0$ in order to depress the convection, while it must be set in the region $-A \leqslant Z < 0$ for $\beta_S < 0$. Eqs. (5), (7) and (27) retain the same forms even when β_S, c_0 and c_1 are, respectively, replaced with $-\beta_S$, c_1 and c_0. As a result, we treat only the case of $\beta_S > 0$ in this section, because the calculated result for $\beta_S < 0$ should be the same as that for $\beta_S > 0$. The concentration difference Δc must be small, taking account of the concentration dependence of D. Therefore, α's are

assumed to be 0, 1 or 10, respectively, which correspond to $\Delta c = 0$ at.%, 1 at.% or 10 at.%, because the concentration accuracy of electron probe microanalysis, which is often used for concentration measurement in solids, is 0.1 at.% at most. The other parameters are $\delta = 0.1$, and $Ha = 0$ or 40.

Since the experimental period of time for diffusion is $\tau = 1000$ s at most in our research [2], the transient calculations were performed until $t = 2$. Fig. 7 shows $U_{\max}(0,t)$, defined as the magnitude of the maximum velocity as a function of Ha and t, for $Gr = 100$. We can see that $U_{\max}(0,t)$ is constant regardless of α at $2 \times 10^{-3} < t < 1$ and $U_{\max}(0,t)$ when $\alpha = 10$ is lower than that when $\alpha = 0$ or 1 at $t > 1$. The reason for the difference at $t > 1$ is that the steep positive concentration gradient in the vicinity of the $Z = 0$ plane in this melt, where the initial concentration distribution is set to be a stepwise function of Z, weakens the driving force of the convection. The region with the steep concentration gradient affects the convection behavior by acting as a stagnant layer. The calculated concentration and velocity fields in the melt are shown in Fig. 8. At the beginning of diffusion, a weak convection roll appears in the stagnant layer due to the steep concentration gradient in the vicinity of the $Z = 0$ plane, and two strong convective rolls are generated from the layer. $U_{\max}(Ha,t)$ reaches a certain constant value, and subsequently, the width of the stagnant layer increases and the convective rolls move toward $Z = \pm A$ with time.

Fig. 9 shows the average concentration gradient on the $Z = 0$ plane under gravity, G_C^*, as a function of time. The deviation of the diffusion coefficient obtained under gravity D^* from the true value can be evaluated by

$$\varepsilon(t) = (D^* - D)/D = (G_C/G_C^*)^2 - 1 \approx (G_{C0}/G_C^*)^2 - 1, \tag{28}$$

because the initial concentration distribution, Eq. (27), is different from the value obtained using Eq. (24), but

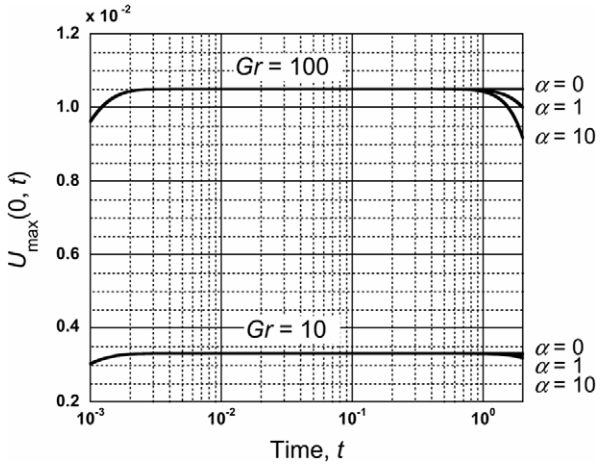

Fig. 7. $U_{\max}(0,t)$ for $Gr = 10$ and 100 with $n = 2$.

$G_{C0}(t) = G_C^*(t)$ for $Gr = 0$ converges to $1/2\sqrt{\pi t}$ within the deviation of 10^{-3} at $t = 2$. As a result of the calculation, both $\varepsilon(1)$ and $\varepsilon(2)$ are found to be less than 10^{-3} under the convection-damped condition, such as ($\alpha = 1$, $Ha = 0$), ($\alpha = 10$, $Ha = 0$), or ($\alpha = 0$, $Ha = 40$), while $\varepsilon(1) = 0.85$ and $\varepsilon(2) = 0.88$ for ($\alpha = 0$, $Ha = 0$). The damping effect of the concentration gradient on the flow velocity becomes obvious with the increase of α, as expected from Eq. (5). In the case of a laminar flow condition for $Gr > 100$, $\varepsilon(t)$ will increase with the increase of Gr for the same α, and larger Ha will be required to damp the convection more effectively. The maximum concentration gradient will decrease to zero with time, and the maximum velocity will increase with the decrease of the width of the stagnant layer under the condition $|\alpha \nabla_N C| < |\nabla_N T|$. Finally, the thermal convection will become a dominant flow under the steady-state condition discussed in Section 4.1. The present calculation supports the validity of the experimental result that the concentration gradient in the vicinity of the joint surface of the diffusion couple damped the buoyancy convection [14].

Are there no other volumetric forces in conducting melt under a static magnetic field than gravity and Lorentz forces? A steep temperature gradient in a specimen may induce some effects such as the thermoelectric voltage known as the Seebeck effect. This effect occurs between a liquid and a solid of a metal if the Seebeck coefficients are different. Kaneda et al. pointed out a possibility, on the basis of a numerical simulation, that Lorentz force, which is induced by the Seebeck current under a static magnetic field, yields convection even under a zero-gravity condition in the case of the container material being electrically conductive [15]. In other words, convection is not induced by the thermoelectrical effect in a melt in an electrically insulating container. The experimental result of a diffusion measurement performed by Mathiak et al. [9] showed no obvious dependence of magnetic field on diffusivity up to 14 T in In–Sn melt in an insulating container. Therefore, we can consider that the effect of externally applied static magnetic field on the fluid behavior is simply due to Lorentz force of conducting melt in an insulating container, as assumed in the present calculation.

Consequently, a diffusion coefficient with high accuracy can be obtained experimentally for metal or semiconductor melt under the terrestrial condition if the experiment is performed such that the fluid-dynamical condition is satisfied with large α and Ha, and a segregation effect on the concentration distribution in the specimen can be suppressed during a quench process after the diffusion. Small Δc is preferable for measuring D experimentally, taking a concentration dependence of the coefficient into account, while small α causes a decrease in the period in which the concentration gradient in the vicinity of $Z = 0$ affects the convection. Thus, a diffusion couple with a large β_S/β_T ratio is suitable for the measurement.

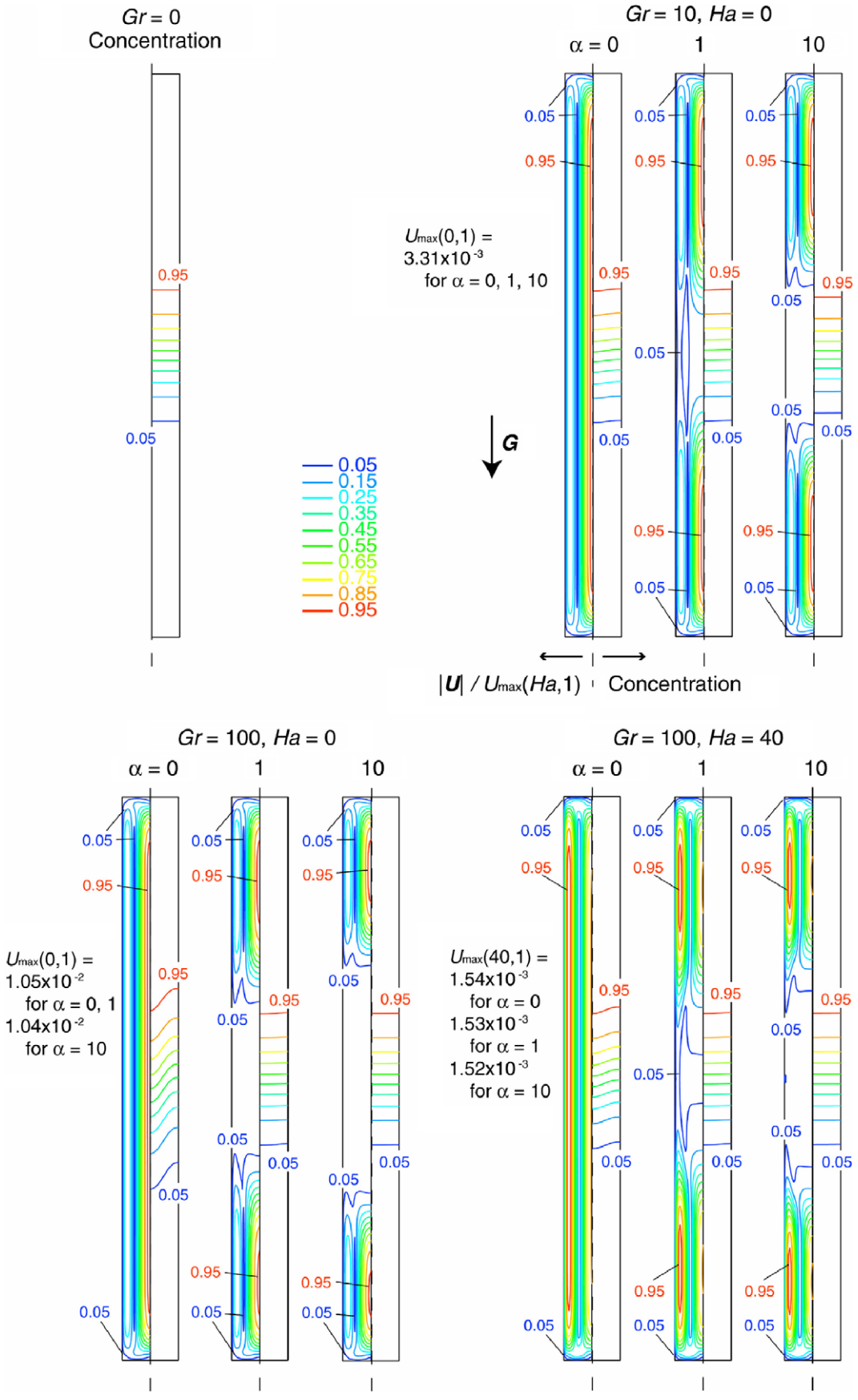

Fig. 8. Contour plots of magnitude of velocity and concentration fields in $X = 0$ planes at $t = 1$ for $\boldsymbol{G} \| \boldsymbol{e}_Z$.

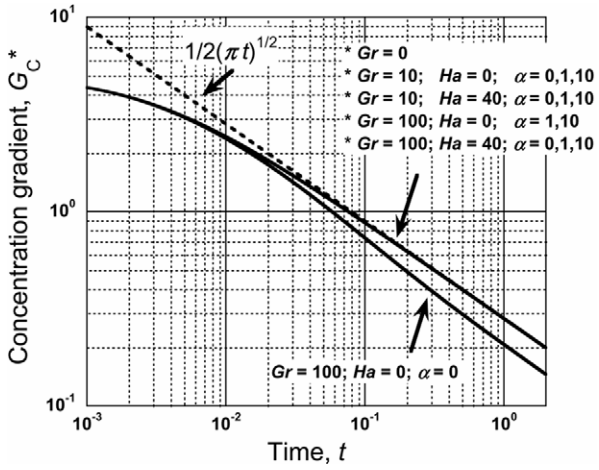

Fig. 9. Average concentration gradient on $Z = 0$ plane, G_C^*, as a function of time.

5. Conclusion

The application of a uniform magnetic field is a potential method for obtaining an accurate measurement of the diffusion coefficient in an electrically conductive fluid, and is also a promising substitute of the microgravity environment. The results of the numerical simulation reveal the following necessary conditions for a diffusion experiment under a static magnetic field. (1) The melt must have a small radius with a large aspect ratio. (2) The melt axis must be parallel to gravity and the temperature gradient along the axis must be small. (3) A uniform and strong static magnetic field must be applied perpendicular to the melt axis. (4) A high-concentration alloy must be set at the upper side in the diffusion couple for $\alpha > 0$, whereas the alloy must be set at the lower side for $\alpha < 0$. (5) Large α is effective for damping the convection.

Acknowledgements

This research was supported by the Ministry of Education, Culture, Sports, Science and Technology, Grant-in-Aid for Scientific Research (C), 13650806, 2001, by a "Fund for Basic Utilization" of ISAS, and by a grant from Japan Space Forum. The authors wish to thank Masaru Sato from FLUENT Inc. for technical advises for FIDAP.

References

[1] T. Masaki, T. Fukazawa, S. Matsumoto, T. Itami, S. Yoda, Measurements of diffusion coefficients of metallic melt under microgravity—current status of the development of shear-cell technique towards JEM on ISS, Measur. Sci. Technol. 16 (2005) 327–335.
[2] T. Miyake, Y. Inatomi, K. Kuribayashi, Measurement of diffusion coefficient in liquid metal under static magnetic field, Jpn. J. Appl. Phys. 41 (7A) (2002) L811–L813.
[3] Y. Malmejac, G. Frohberg, Mass transport by diffusion, in: H. Walter (Ed.), Fluid Sciences and Materials Sciences in Space, Springer, Berlin, 1986, pp. 159–190.
[4] T. Itami, H. Aoki, M. Kaneko, M. Uchida, A. Shisa, S. Amano, O. Odawara, T. Masaki, H. Oda, T. Ooida, S. Yoda, Diffusion of liquid metals and alloys—the study of self-diffusion under microgravity in liquid Sn in the wide temperature range, J. Jpn. Soc. Microgravity Appl. 15 (4) (1998) 225–232.
[5] R.A. Herring, W.M.B. Duval, R.W. Smith, K.S. Rezkellah, S. Varma, R.F. Redden, B.V. Tryggvason, Recent measurements of experiment sensitivity to g-jitter and their significance to ISS facility development, J. Jpn. Soc. Microgravity Appl. 16 (4) (1999) 234–244.
[6] K. Kinoshita, H. Kato, S. Matsumoto, S. Yoda, J. Yu, M. Natsuisaka, T. Masaki, N. Koshikawa, Y. Nakamura, T. Nakamura, A. Ogiso, S. Amano, K. Goto, Y. Arai, T. Fukazawa, M. Kaneko, T. Itami, InAs–GaAs interdiffusion measurements, J. Jpn. Soc. Microgravity Appl. 17 (2) (1999) 57–63.
[7] D.T.J. Hurle, E. Jakeman, C.P. Johnson, Convective temperature oscillations in molten gallium, J. Fluid Mech. 64 (1974) 565–576.
[8] R.W. Series, D.T.J. Hurle, The use of magnetic fields in semiconductor crystal growth, J. Cryst. Growth 113 (1-2) (1991) 305–328.
[9] G. Mathiak, G. Frohberg, Interdiffusion and convection in high magnetic fields, Cryst. Res. Technol. 34 (2) (1999) 181–188.
[10] V. Botton, P. Lehmann, R. Bolcato, R. Moreau, A new measurement method of solute diffusivities based on MHD damping of convection in liquid metals and semi-conductors, Energy Convers. Manage. 43 (3) (2002) 409–416.
[11] M.S. Engelman, FIDAP 8.0, Fluent Inc. Lebanon, NH, USA, 1998.
[12] E.A. Brandes, G.B. Brook, Smithells Metals Reference Book, seventh ed., Butterworth-Heinemann, Oxford, 1992 (Chapter 14).
[13] D.H. Kim, P.M. Adornato, R.A. Brown, Effect of vertical magnetic field on convection and segregation in vertical Bridgman crystal growth, J. Cryst. Growth 89 (2-3) (1988) 339–356.
[14] S. Suzuki, K.H. Kraatz, G. Frohberg, Diffusion experiments in liquid Sn–Bi and Al–Ni systems with a stable density layering using the foton shear cell under 1G conditions, Microgravity Sci. Technol. XVI (2005) 120–126.
[15] M. Kaneda, T. Tagawa, H. Ozoe, K. Kakimoto, Y. Inatomi, Natural convection of liquid metal with and without Seebeck effect, in: P. Cheng (Ed.), Proceedings of Symposium on Energy Engineering in the 21st Century (SEE2000), Vol.1, Begell, 2000, pp. 302–309.